RSC Advances

PAPER

View Article Online
View Journal | View Issue

Cite this: *RSC Adv.*, 2021, **11**, 23700

Synthesis of vertical WO_3 nanoarrays with different morphologies using the same protocol for enhanced photocatalytic and photoelectrocatalytic performances†

Jingjing Li,[ab] Chenpeng Guo,[ab] Lihua Li,[ab] Yongjun Gu,[ab] BoK.-Hee Kim[ac] and Jinliang Huang *[ab]

Received 22nd April 2021
Accepted 23rd June 2021

DOI: 10.1039/d1ra03149j

rsc.li/rsc-advances

Tungsten trioxide (WO_3) nanoarrays with different morphologies were successfully synthesized by a hydrothermal method on an FTO substrate. Various nanostructures of WO_3 including nanoflakes, nanoplates, nanoflowers and nanorods were obtained by adjusting only the acidity of the precursor solution. XRD patterns confirmed that the as-prepared orthorhombic $WO_3 \cdot 0.33H_2O$ transformed to the monoclinic WO_3 phase under annealing at 500 °C. UV-Vis absorbance spectroscopy indicated that the absorption edge of WO_3 nanoflowers exhibited a slight red-shift compared to other morphologies of WO_3. The obtained WO_3 nanoflower arrays exhibit the highest photocurrent density and photocatalytic degradation activity towards methylene blue. Finally, the mechanism of the photocatalytic degradation of methylene blue by WO_3 is discussed.

1 Introduction

Methylene blue (MB) is a type of water-soluble polycyclic aromatic dye, which is extensively used in dyestuff, textile and dyeing industry.[1] The dye wastewater with large chromaticity and high organic concentration discharged from the dyestuff and textile industry is considered a dangerous pollutant to the environment. Semiconductor photocatalysis (PC) and photoelectrocatalysis (PEC) have been proved to be efficient and promising for the degradation of organic contaminants.[2–4] It is worth noting that PEC is the combination of photocatalysis with electrocatalysis technologies by applying a biased voltage, which can maximize the utilization of photocatalysts and is a more attractive method in degrading organic pollutants.[5] Tungsten trioxide (WO_3) as a promising n-type semiconductor has been extensively researched in the photocatalysis field due to its remarkable stability in acid aqueous solutions, high electron mobility, resistibility to light corrosion, moderate band gap and low cost.[6]

The morphology and structure of the WO_3 materials have critical influence on the photocatalytic and electrocatalytic properties.[7] Extensive research efforts have been done to synthesize numerous morphological WO_3 materials *via* different methods, such as one-dimensional (1D) nanostructured nanorods (NRs), nanowires (NMs) and nanotubes (NTs),[8–10] two-dimensional (2D) nanostructured nanoflakes (NFs), and nanoplates (NPs).[11,12] However, there are relatively fewer studies on the synthesis of three-dimensional (3D) materials. Also, the effects of the WO_3 array crystal morphology with various dimensions on the photocatalytic properties have not been systematically studied.

At present, WO_3 crystals with different morphologies are typically obtained by selecting different synthesis methods,[13–16] or by changing the operation parameters, including modifications to the precursor, structure-directing agents, surfactants and solvents.[17–20] Due to the composition of precursors and the change in the chemical reaction environment, the obtained WO_3 crystals showed poor reproducibility on the array film quality, photocatalytic and photoelectrocatalytic performances.[21,22] Therefore, it is necessary to develop an efficient and highly reproducible method to produce morphology-controlled WO_3 crystals. The metatungstate anion $[H_2W_{12}O_{40}]^{6-}$ of the ammonium metatungstate (AMT), known as a KEGGIN anion structure with a "tetrahedral cavity" in its center, endows the AMT with exceptional structural configurations.[23] The unique molecular structure makes AMT relatively stable under ambient conditions.[24]

In this study, chemically stable AMT was used as the tungsten source, and a series of diversified morphology WO_3

[a]*School of Materials Science and Engineering, Henan University of Science and Technology, Luoyang 471023, China. E-mail: huangjl@haust.edu.cn*

[b]*Provincial and Ministerial Co-construction of Collaborative Innovation Center for Non-ferrous Metal New Materials and Advanced Processing Technology, Luoyang 471023, China*

[c]*Division of Advanced Materials Engineering, Hydrogen and Fuel Cell Research Center, Chonbuk National University, Jeonbuk, South Korea*

† Electronic supplementary information (ESI) available. See DOI: 10.1039/d1ra03149j

photocatalysts were successfully synthesized in the same reaction system. The WO_3 with different morphologies including nanoflakes, nanoplates, nanoflowers, and nanorods were obtained by only adjusting the acidity of the hydrothermal precursor solution. Their photoelectric and photocatalytic properties were investigated. Moreover, the mechanism of photocatalytic degradation was investigated.

2 Materials and methods

2.1 Preparation of WO_3 arrays with different morphologies

All reagents were of analytical grade and used without any further purification. An FTO glass substrate (2×5 cm^2) was cleaned using acetone, absolute ethanol and deionized water, separately. 0.5 g of ammonium metatungstate hydrate ($(NH_4)_6H_2W_{12}O_{40}\cdot xH_2O$) was dissolved in 40 mL deionized water by magnetic stirring. 1–7 mL of 3 M concentrated hydrochloric acid (HCl) was slowly added to the above solution and stirred for 5 min. 2 mL of hydrogen peroxide (H_2O_2, 30%) was dropped into the solution and adjusted its volume to 50 mL using deionized water, followed by stirring for 1 h. The reaction solution was then poured into a 43 mL Teflon-lined stainless steel autoclave with the FTO substrate and kept at 160 °C for 4 h. After reaction, the autoclave was cooled down to room temperature. The product was filtered and dried at 60 °C for 10 h. Finally, the samples were annealed at 500 °C for 1 h. The as-prepared WO_3 arrays were referred to as W-x (x (mL) = 1, 2, 4, 5, 6, and 7), where x is the volume of HCl.

2.2 Characterization

X-ray diffraction (XRD) measurements were conducted on a Bruker D8 Advanced diffractometer with Cu Kα radiation. Field emission scanning electron microscopy (FESEM) and energy dispersive X-ray spectroscopy (EDS) were determined using JEOL JSM-7800F instruments. UV-Vis diffuse reflectance spectra (UV-Vis DRS) were recorded using a UV-2600 spectrometer. Photoluminescence (PL) spectra were obtained on a Hitachi F-280 fluorescence spectrophotometer at the excitation wavelength at 325 nm.

2.3 Photoelectrochemical measurements

The photoelectrochemical measurements of WO_3 arrays were performed in a CHI660E electrochemical workstation using a standard three-electrode cell. The as-synthesized WO_3 arrays were used as the working electrodes, a platinum net was used as the counter electrode and Ag/AgCl was used as the reference electrode. The aqueous solution of 0.5 M Na_2SO_4 was used as an electrolyte. The illumination source used was a 500 W Xe arc lamp (CEL-HXF300) with a AM 1.5 G filter. The measured potentials *vs.* Ag/AgCl were converted to the potentials *vs.* reversible hydrogen electrode (RHE) using the following Nernst equation:[25]

$$E_{RHE} = E_{Ag/AgCl} + 0.059pH + E^0_{Ag/AgCl}$$

2.4 Photocatalytic and photoelectrocatalytic degradation measurements

The degradation experiment was carried out using the same three-electrode system described above. The photocatalytic and photoelectrocatalytic activity of these WO_3 arrays with different morphologies were evaluated by the degradation of methylene blue (MB). The initial concentration of MB was 10 mg L^{-1}, and the electrolyte was 0.1 mol L^{-1} Na_2SO_4. First, magnetic stirring was carried out in dark for 30 min to achieve the equilibrium of adsorption and desorption. After certain time intervals during irradiation, 3 mL of the degradation was taken to analyze the concentration MB using a UV-Vis spectrophotometer. The main active species in the photodegradation process were analyzed by adding different radical scavengers. Here, 1 mmol ammonium

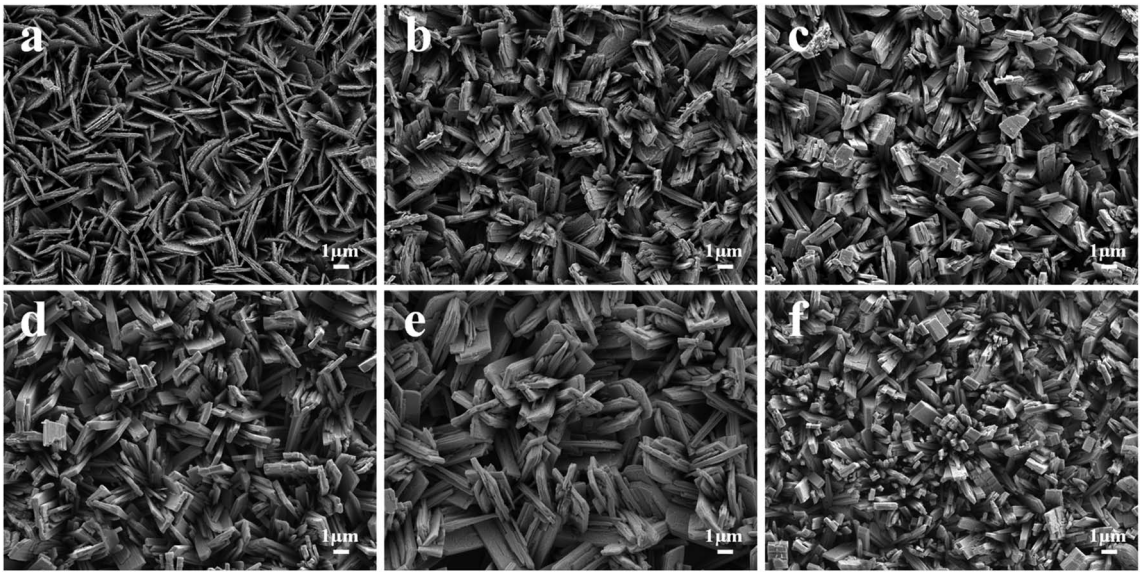

Fig. 1 FESEM images of (a) W-1, (b) W-2, (c) W-4, (d) W-5, (e) W-6, (f) W-7.

oxalate (AO), methanol (MT), and *p*-benzoquinone (*p*-BQ) were used as a hole (h^+) scavenger, hydroxyl radical ($\cdot OH$) scavenger, and superoxide radical ($\cdot O_2^-$) scavenger, respectively.

3 Result and discussion

3.1 Morphology and structure

The WO_3 arrays with different morphologies after being annealed were confirmed by FESEM, as shown in Fig. 1. It can be seen that the WO_3 nanoarrays are nearly vertically aligned on the FTO substrates, and exhibited strong adhesion to the FTO substrate. When the volume of HCl was 1 mL, it showed a uniform array of nanoflake structure. The widths and thicknesses of the nanoflakes were about 2.5 μm and 150 nm, respectively (Fig. 1a). With an increase in the volume of HCl, the thicknesses of the nanoflakes increased, while the morphology changed to a nanoplate array structure (Fig. 1b–d). When the volume of HCl is 5 mL, regular uniform WO_3 nanoplates were obtained, and the thicknesses increased to 300 nm (Fig. 1d). As the volume of HCl is added up to 6 mL, the morphology of WO_3 turned into nanoflowers and each nanoflower is regularly composed of six nanoplates of equal size (Fig. 1e). However, when the amount of HCl increases to 7 mL, the morphology of WO_3 turns into a nanorod array structure (Fig. 1f).

Fig. 2 shows the low-magnification FESEM image and the EDS pattern of the W-6 sample. As shown in Fig. 2b, there were no impurity elements except W and O, indicating that the sample prepared by the hydrothermal reaction is tungsten oxide. The preparation of WO_3 with different morphologies on FTO is illustrated in Fig. 3. The pH value affects the solubility of a substance and influences the growth of the crystal in a hydrothermal reaction.[26] Therefore, different WO_3 morphologies were obtained by adjusting the pH values of the precursor solutions.

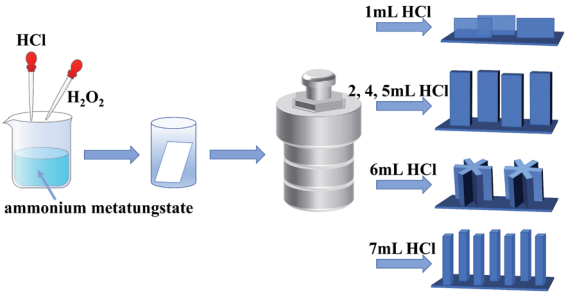

Fig. 3 Schematic of the WO_3 arrays on FTO.

Fig. 4 shows the XRD patterns of the as-prepared and annealed WO_3 nanoarrays. All the as-prepared arrays obtained by the hydrothermal reaction with different pH values were orthorhombic $WO_3 \cdot 0.33H_2O$ (JCPDS no. 54-1012). The diffraction peaks with 2θ values at 18.1°, 22.9°, 24.1°, 28.1° and 36.6°

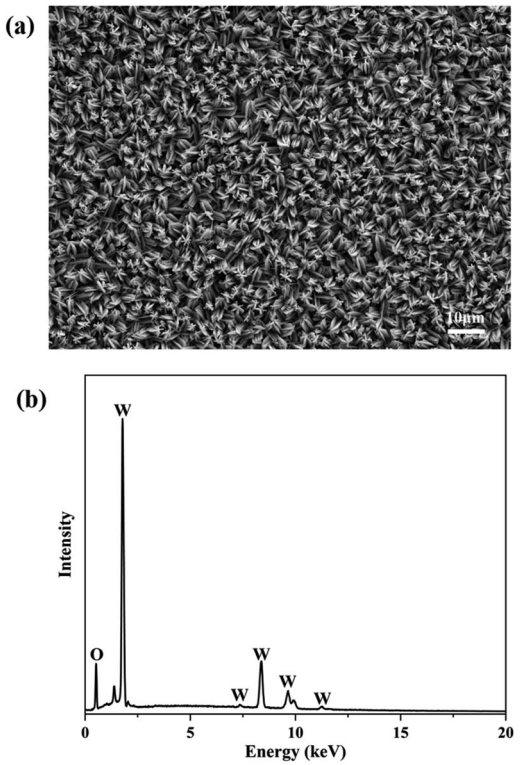

Fig. 2 (a) Low-magnification FESEM image and (b) EDS pattern of W-6.

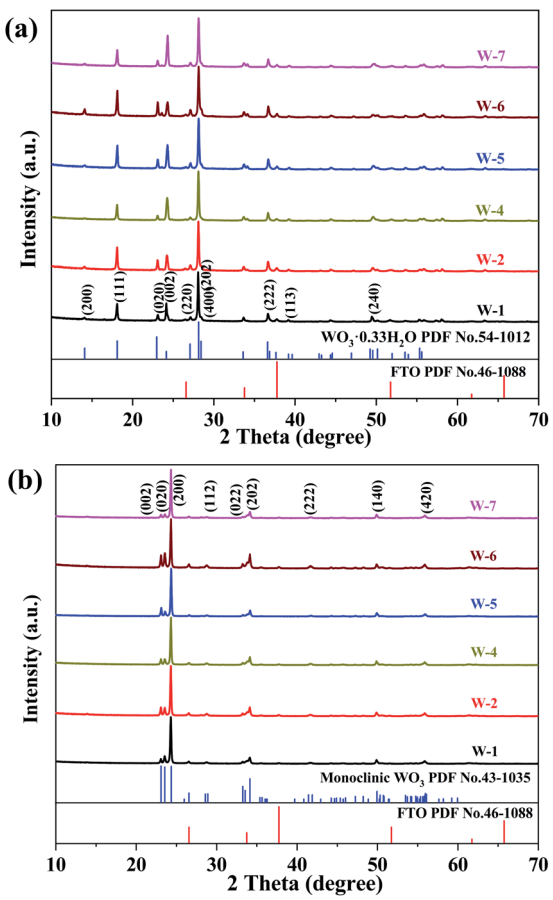

Fig. 4 XRD patterns of the WO_3 arrays (a) as-prepared and (b) annealed.

were indexed to the (111), (020), (002), (202) and (222) facets, respectively (Fig. 4a). After being annealed, the diffraction peaks of all samples are indexed to the monoclinic WO_3 (JCPDS no. 43-1035), and three peaks at 23.1°, 23.5° and 24.3° corresponded to the (002), (020) and (200) facets (Fig. 4b). The intensive and sharp diffraction feature of WO_3 samples showed excellent crystallinity.[27] The chemical composition of orthorhombic $WO_3 \cdot 0.33H_2O$ changed and transformed to a stable monoclinic WO_3 after annealing.[28] According to the XRD patterns, the (002), (020) and (200) facets are the main features in monoclinic WO_3. The surface energy order was (002) > (020) > (200), which indicates that the (002) facet in monoclinic WO_3 has the largest surface energy as the most reactive surface.[29] Based on the peak areas of the (002), (020) and (200) facets, the proportion of the (002) facet was calculated. The calculated proportions of the exposed (002) facet of WO_3 are about 6.96% (W-1), 9.77% (W-2), 9.53% (W-4), 13.06% (W-5), 14.81% (W-6), 6.92% (W-7). Therefore, the hexagonal flower-like (W-6) WO_3 exposes more (002) facets.

3.2 Optical properties

The UV-Vis absorption spectra and PL spectra of the annealed WO_3 arrays are illustrated in Fig. 5. The inset in Fig. 5a is the corresponding Tauc plots of band gap. These four different morphology arrays with nanoflake (W-1), nanoplate (W-5), nanoflower (W-6), and nanorod (W-7) have almost similar absorption spectra, and the absorption edges is at *ca.* 466 nm.

The optical band gap (E_g) of the WO_3 samples could be calculated using the equation:[30]

$$(\alpha h\nu)^{1/2} = A(h\nu - E_g)$$

where α is the absorption coefficient, h is the Planck's constant, ν is the frequency of the radiation, and A is a constant. The calculated E_g values of WO_3 nanoflakes (W-1), nanoplates (W-5), nanoflowers (W-6), and nanorods (W-7) are 2.66 eV, 2.65 eV, 2.63 eV, and 2.68 eV, respectively, indicating that the morphology had little effect on the band gap of WO_3. All the samples are consistent with the energy gap of monoclinic WO_3 (2.6–2.8 eV).[31] Moreover, the absorption edge of WO_3 nanoflowers exhibits a slight redshift in the UV-Vis spectrum.

The recombination of photogenerated charge carriers was evaluated *via* PL measurements.[32] Fig. 5b shows the PL spectra of WO_3 arrays excited at 325 nm light at room temperature. It can be seen that the WO_3 nanoflowers (W-6) showed a lower fluorescence peak, indicating that the recombination probability of photo-excited electron hole pairs is lower. In one word, the more (002) facet of the WO_3 nanoflower (W-6) is beneficial to the separation of photo-excited electrons and holes, and more photogenerated carriers participate in the photoelectrocatalytic reaction.

3.3 Photoelectrochemical performances

The linear sweep voltammograms (LSV) (Fig. 6a) and amperometry *I–t* curve (Fig. 6b) of the annealed WO_3 were measured as

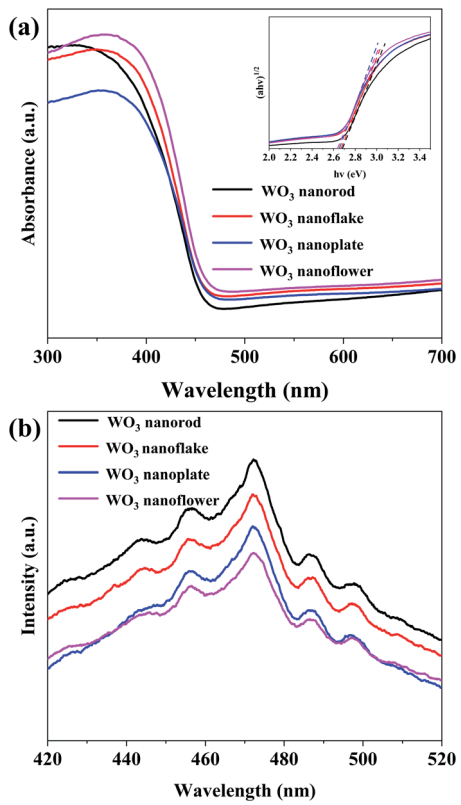

Fig. 5 (a) UV-Vis absorption spectra and (b) room temperature PL spectra of the annealed WO_3 arrays.

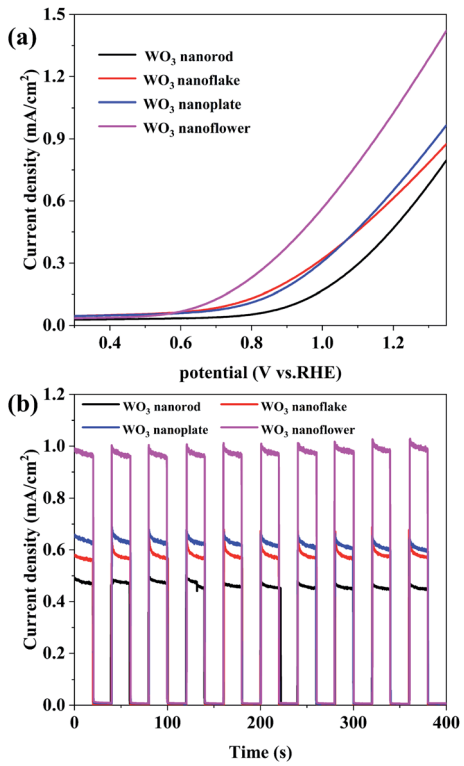

Fig. 6 (a) Linear sweep voltammetry (LSV) curves of the WO_3 arrays. (b) Amperometric *I–t* curve of the WO_3 arrays at 1.2 V *vs.* RHE.

photoanode materials. The photocurrent density of the WO_3 nanorod (W-7) photoanode is 0.43 mA cm^{-2} at 1.23 V *vs.* RHE, while that of the nanoflake (W-1) and nanoplate (W-5) were 0.67 and 0.72 mA cm^{-2}, indicating that the morphology engineering of the WO_3 arrays has important implications on PEC performance. Moreover, the nanoflower (W-6) exhibits the highest photocurrent density, reaching 1.10 mA cm^{-2} at 1.23 V *vs.* RHE. The photocurrent increase is mainly due to the higher exposed (002) facets, and 3D nanoflowers exhibit unique optical properties, which provide more reaction sites and enhanced charge transport.

The photocurrent density–time (*I*–*t*) curves shown in Fig. 6b are obtained to determine the photocurrent stability of the WO_3 arrays. Clearly, the photocurrent densities get close to zero when the light is off, and they increase rapidly and stabilize at a certain value under illumination. All WO_3 arrays showed fast and uniform photocurrent response.[33] The four photoanode have similar curves and more photocurrent stability, indicating that it a good method to obtain stable WO_3 arrays with ammonium metatungstate. Fig. S1† shows the electrochemical impedance spectroscopy (EIS) of the WO_3 arrays, and the semicircle radius in the Nyquist curve reflects the charge transfer at the electrode/electrolyte interface. The WO_3 nanoflower shows a smaller semicircle radius, which indicates lower charge transfer resistance and higher separation efficiency of photogenerated electron hole pairs.

3.4 Photocatalytic and photoelectrocatalytic activity

The results of MB degradation are shown in Fig. 7. Fig. 7a and b show the photocatalytic (PC) activity (illumination without bias) of the WO_3 arrays and the first order kinetics curve fitting. It can be seen that the WO_3 nanoflowers have the highest photocatalytic activity, which degrade 66.39% of MB within 80 min. The degradation efficiencies of WO_3 nanoplates,

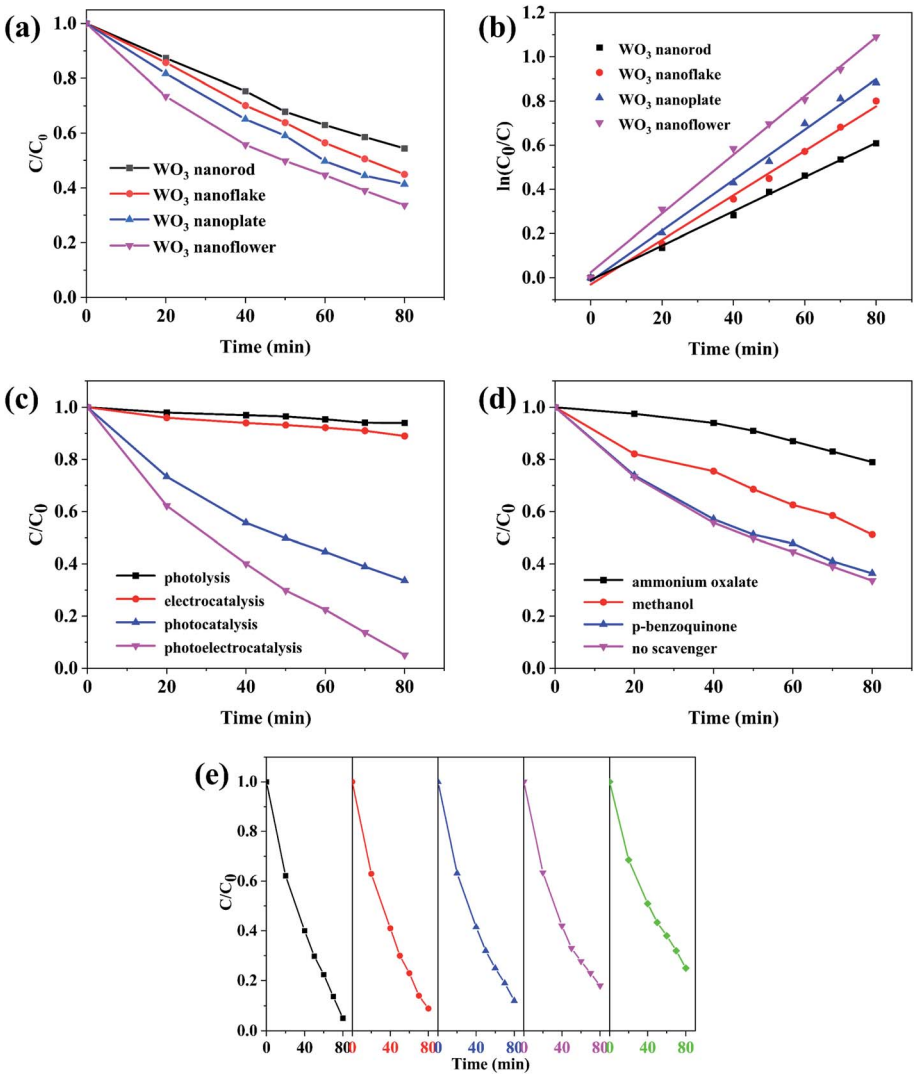

Fig. 7 (a) PC degradation of MB and (b) the corresponding kinetic curves by different WO_3 morphology films. (c) Degradation of MB *via* various techniques using WO_3 nanoflowers. (d) Photocatalytic degradation of MB over WO_3 nanoflowers using different scavengers. (e) Durability of the WO_3 nanoflower photoanode for the degradation of MB.

nanoflakes and nanorods are 58.64%, 55.09% and 45.59%, respectively, proving that the photocatalytic activity is decided by the morphology. The photocatalytic degradation of MB by WO_3 arrays follow the linear first-order kinetics equation:[34]

$$\ln(C_0/C) = kt$$

where k is the constant of the degradation reaction rate, which could be used to compare the performances of catalysts. The highest PC degradation reaction rate of the WO_3 nanoflowers was 0.013 min^{-1}, which is 1.86 times higher than that of WO_3 nanorods (0.007 min^{-1}). The degradation rate of methylene blue by TiO_2 nanorods reached 25% within 5 h,[35] while the pure ZnO decolorized 35% of MB dye after 1.5 h.[36] The photocatalytic degradation activity of WO_3 to MB in visible light was higher than that of other reported metal oxide, which indicates that WO_3 has a great potential for MB degradation.

Fig. 7c shows the degradation of MB with various techniques using WO_3 nanoflowers. After 80 min, only 6% of MB was removed by direct photolysis, showing that MB is not easy to degrade under solar illumination. The photoelectrocatalysis (PEC) degradation rate of the MB increased to 94.9% after applying an electrical bias potential of 0.8 V to the WO_3 nanoflower array electrode, which can be attributed to avoid the recombination of electron–hole by electrical bias potentials. Therefore, the synergistic effects of photocatalysis (PC) and electrooxidation (EC) can significantly improve the degradation efficiency of MB.

The effects of different radical scavengers on the photocatalytic degradation of MB are shown in Fig. 7d. The photocatalytic efficiency noticeably decreased after adding ammonium oxalate, indicating that h^+ was the dominant active species. The degradation efficiency of MB decreased by 17.59% (to 48.8%) after methanol addition, this suggests that $\cdot OH$ could have some effects on photocatalytic efficiency. When *p*-benzoquinone was added to the reaction solution, the photocatalytic activity was similar to that of the sample without scavengers, confirming that $\cdot O_2^-$ was not an active species for MB degradation. The main reason may be that the conduction band of WO_3 is more positive than that of $E(O_2/\cdot O_2^-)$ (−0.33 eV/NHE),[37] so electrons could not react with O_2 to generate $\cdot O_2^-$. The valence band of WO_3 is more positive than $E(\cdot OH/OH^-)$ and $E(\cdot OH/H_2O)$, and the holes in the VB of WO_3 can react with OH^- and H_2O_2 to generate $\cdot OH$.[38] Moreover, the photogenerated holes generated by WO_3 can degrade MB directly.

The photoelectrocatalysis stability of the WO_3 nanoflower array for MB degradation was measured by the cyclic experiment (Fig. 7e). After five cycles, the degradation rate of WO_3 array was 79%, decreased by 16.7%. Moreover, the XRD spectra and FESEM images of WO_3 after cyclic degradation are shown in Fig. S2.† There is no difference in phase and morphology before and after catalysis. The results indicate that the WO_3 arrays is stable.

4 Conclusions

Different morphologies of vertically WO_3 nanoarrays were successfully synthesized on FTO substrates *via* a one-step hydrothermal process. The morphology of WO_3 was sensitive to the acidity of the solution and changed from nanoflakes, nanoplates and nanoflowers to nanorods as the volume of HCl increased from 1 mL to 7 mL. Particularly, WO_3 nanoflowers demonstrated the highest photocurrent density performance compared to other morphologies. The enhanced charge transport and the specific WO_3 hexagonal nanoflower contributes to the significant PEC activity. Moreover, the WO_3 nanoflower array exhibited better performance than other morphologies in MB photocatalytic degradation, which demonstrated that the morphology of WO_3 plays an important role in the PEC and photocatalytic performance. The different scavenger degradation MB in WO_3 nanoflowers confirm that the h^+ radical species play a vital role in the reaction.

Conflicts of interest

There are no conflicts to declare.

Acknowledgements

This work has been financially supported by the Provincial and Ministerial Co-construction of Collaborative Innovation Center for Non-ferrous Metal New Materials and Advanced Processing Technology.

References

1 M. Rafatullah, O. Sulaiman, R. Hashim and A. Ahmad, *J. Hazard. Mater.*, 2010, **177**, 70–80.
2 S. Pal, S. Maiti, U. N. Maiti and K. K. Chattopadhyay, *CrystEngComm*, 2015, **17**, 1464–1476.
3 W. Zhang, B. S. Naidu, J. Z. Ou, A. P. O'Mullane, A. F. Chrimes, B. J. Carey, Y. Wang, S.-Y. Tang, V. Sivan, A. Mitchell, S. K. Bhargava and K. Kalantar-zadeh, *ACS Appl. Mater. Interfaces*, 2015, **7**, 1943–1948.
4 B. M. Pirzada, Pushpendra, R. K. Kunchala and B. S. Naidu, *ACS Omega*, 2019, **4**, 2618–2629.
5 N. Baram, D. Starosvetsky, J. Starosvetsky, M. Epshtein, R. Armon and Y. Ein-Eli, *Electrochem. Commun.*, 2007, **9**, 1684–1688.
6 G. Zheng, J. Wang, H. Liu, V. Murugadoss, G. Zu, H. Che, C. Lai, H. Li, T. Ding and Q. Gao, *Nanoscale*, 2019, **11**, 18968–18994.
7 B. Miao, W. Zeng, Y. Mu, W. Yu, S. Hussain, S. Xu, H. Zhang and T. Li, *Appl. Surf. Sci.*, 2015, **349**, 380–386.
8 J. Wang, E. Khoo, P. S. Lee and J. Ma, *J. Phys. Chem. C*, 2008, **112**, 14306–14312.
9 K. Zhu, H. He, S. Xie, X. Zhang, W. Zhou, S. Jin and B. Yue, *Chem. Phys. Lett.*, 2003, **377**, 317–321.
10 P. M. Rao, I. S. Cho and X. Zheng, *Proc. Combust. Inst.*, 2013, **34**, 2187–2195.
11 G. Zhang, W. Guan, H. Shen, X. Zhang, W. Fan, C. Lu, H. Bai, L. Xiao, W. Gu and W. Shi, *Ind. Eng. Chem. Res.*, 2014, **53**, 5443–5450.
12 D. Chen, X. Hou, H. Wen, Y. Wang, H. Wang, X. Li, R. Zhang, H. Lu, H. Xu and S. Guan, *Nanotechnology*, 2009, **21**, 035501.

13 M. B. Johansson, B. Zietz, G. A. Niklasson and L. Österlund, *J. Appl. Phys.*, 2014, **115**, 213510.
14 H. Habazaki, Y. Hayashi and H. Konno, *Electrochim. Acta*, 2002, **47**, 4181–4188.
15 J.-H. Ha, P. Muralidharan and D. K. Kim, *J. Alloys Compd.*, 2009, **475**, 446–451.
16 N. Le Houx, G. Pourroy, F. Camerel, M. Comet and D. Spitzer, *J. Phys. Chem. C*, 2010, **114**, 155–161.
17 S. G. Kumar and K. K. Rao, *Appl. Surf. Sci.*, 2017, **391**, 124–148.
18 S. Adhikari, D. Sarkar and H. S. Maiti, *Mater. Res. Bull.*, 2014, **49**, 325–330.
19 A. Yan, C. Xie, D. Zeng, S. Cai and M. Hu, *Mater. Res. Bull.*, 2010, **45**, 1541–1547.
20 T. Zhang, J. Su and L. Guo, *CrystEngComm*, 2016, **18**, 8961–8970.
21 J. Feng, X. Zhao, B. Zhang, G. Yang, Q. Qian, S. S. K. Ma, Z. Chen, Z. Li and Y. Huang, *Sci. China Mater.*, 2020, **63**, 2261–2271.
22 M. Rashad and A. Shalan, *Appl. Phys. A: Mater. Sci. Process.*, 2014, **116**, 781–788.
23 J. Pavlov, W. Braida, A. Ogundipe, G. O'connor and A. B. Attygalle, *J. Am. Soc. Mass Spectrom.*, 2009, **20**, 1782–1789.
24 S. K. Biswas, J.-O. Baeg, S.-J. Moon, K.-j. Kong and W.-W. So, *J. Nanopart. Res.*, 2012, **14**, 1–12.
25 F. Cui, Y. Zhang, H. A. Fonseka, P. Promdet, A. I. Channa, M. Wang, X. Xia, S. Sathasivam, H. Liu and I. P. Parkin, 2020, arXiv preprint arXiv:2012.09149.
26 X. Su, F. Xiao, J. Lin, J. Jian, Y. Li, Q. Sun and J. Wang, *Mater. Charact.*, 2010, **61**, 831–834.
27 H. J. Ensikat, M. Boese, W. Mader, W. Barthlott and K. Koch, *Chem. Phys. Lipids*, 2006, **144**, 45–59.
28 S. S. Kalanur, Y. J. Hwang, S. Y. Chae and O. S. Joo, *J. Mater. Chem. A*, 2013, **1**, 3479–3488.
29 Y. P. Xie, G. Liu, L. Yin and H.-M. Cheng, *J. Mater. Chem.*, 2012, **22**, 6746–6751.
30 Y. Peng, Q.-G. Chen, D. Wang, H.-Y. Zhou and A.-W. Xu, *CrystEngComm*, 2015, **17**, 569–576.
31 J. Y. Zheng, G. Song, J. Hong, T. K. Van, A. U. Pawar, D. Y. Kim, C. W. Kim, Z. Haider and Y. S. Kang, *Cryst. Growth Des.*, 2014, **14**, 6057–6066.
32 G. Plechinger, P. Nagler, A. Arora, R. Schmidt, A. Chernikov, A. G. Del Águila, P. C. Christianen, R. Bratschitsch, C. Schüller and T. Korn, *Nat. Commun.*, 2016, **7**, 1–9.
33 Y. Hou, F. Zuo, A. P. Dagg, J. Liu and P. Feng, *Adv. Mater.*, 2014, **26**, 5043–5049.
34 F. Liang and Y. Zhu, *Appl. Catal., B*, 2016, **180**, 324–329.
35 R. Wadhene, A. Lamouchi, I. B. Assaker, J. B. Naceur, M. Martínez-Huerta and R. Chtourou, *Inorg. Chem. Commun.*, 2020, **122**, 108298.
36 M. H. Elsayed, T. M. Elmorsi, A. M. Abuelela, A. E. Hassan, A. Z. Alhakemy, M. F. Bakr and H.-H. Chou, *J. Taiwan Inst. Chem. Eng.*, 2020, **115**, 187–197.
37 H. Liang, C. Lv, H. Chen, L. Wu and X. Hou, *RSC Adv.*, 2020, **10**, 45171–45179.
38 X. Li, J. Yu and M. Jaroniec, *Chem. Soc. Rev.*, 2016, **45**, 2603–2636.